Molecular Dynamics Simulations of the Cx26 Hemichannel: Insights into Voltage-Dependent Loop-Gating

Taekyung Kwon,[†] Benoît Roux,[‡] Sunhwan Jo,[§] Jeffery B. Klauda,[¶] Andrew L. Harris,[‖] and Thaddeus A. Bargiello[†*]
[†]Dominic P. Purpura Department of Neuroscience, Albert Einstein College of Medicine, Bronx, New York; [‡]Department of Biochemistry and Molecular Biology, The University of Chicago, Chicago, Illinois; [§]Department of Molecular Biosciences and Center for Bioinformatics, The University of Kansas, Lawrence, Kansas; [¶]Department of Chemical and Biomolecular Engineering, University of Maryland, College Park, Maryland; and [‖]Department of Pharmacology and Physiology, New Jersey Medical School, University of Medicine and Dentistry of New Jersey, Newark, New Jersey

ABSTRACT Loop-gating is one of two voltage-dependent mechanisms that regulate the open probability of connexin channels. The loop-gate permeability barrier is formed by a segment of the first extracellular loop (E1) (the parahelix) and appears to be accompanied by straightening of the bend angle between E1 and the first transmembrane domain (TM1). Here, all-atom molecular dynamics simulations are used to identify and characterize interacting van der Waals and electrostatic networks that stabilize the parahelices and TM1/E1 bend angles of the open Cx26 hemichannel. Dynamic fluctuations in an electrostatic network in each subunit are directly linked to the stability of parahelix structure and TM1/E1 bend angle in adjacent subunits. The electrostatic network includes charged residues that are pore-lining and thus positioned to be voltage sensors. We propose that the transition to the closed state is initiated by voltage-driven disruption of the networks that stabilize the open-state parahelix configuration, allowing the parahelix to protrude into the channel pore to form the loop-gate barrier. Straightening of the TM1/E1 bend appears to be a consequence of the reorganization of the interacting networks that accompany the conformational change of the parahelix. The electrostatic network extends across subunit boundaries, suggesting a concerted gating mechanism.

INTRODUCTION

Voltage is an important parameter regulating the open probability of intercellular channels and undocked hemichannels formed by connexins. Most connexin channels display two distinct voltage-gating processes, termed loop- or slow-gating and V_j- or fast-gating (1,2). Both properties are intrinsic to hemichannels, operating separately by the actions of different voltage sensors and gates (1–3).

Loop-gating, first described in undocked Cx46 hemichannels, results in full channel closure at inside negative potentials (1), suggesting that this is the mechanism that keeps undocked hemichannels closed in plasma membranes. The loop-gate closed state of Cx46 and Cx32 hemichannels is stabilized by divalent cation binding to an extracellular site located outside the channel pore (4,5). In single channel recordings, loop-gating transitions between the open and the fully closed states pass through multiple metastable intermediate states. This gating transition has an appreciable voltage-dependent time constant, in the range of milliseconds to tens of milliseconds (1,3). Similar appearing events are also observed in Cx32, Cx43, Cx45, and Cx40 intercellular channels (3,6–8), suggesting that loop-gating operates in intercellular channels and that the noncovalent interaction between extracellular loops in intercellular channels does not prevent the formation of the loop-gate permeability barrier.

Both intercellular and undocked hemichannels formed by connexins are open in the absence of membrane voltage and adopt closed states with moderate to large polarizations. Consequently, in the simplest case, voltage can be viewed as regulating open channel probability by destabilizing the structure of an open state and stabilizing the structure of a closed state. The slow time constant of both voltage-dependent gating mechanisms observed macroscopically in Cx46, Cx32*43E1, and Cx26, in the order of hundreds of milliseconds to several seconds (1,2,9,10), is consistent with a substantial energy barrier separating open and closed states, according to transition state theory. Therefore, knowledge of the structure and the dynamics of the interactions that stabilize the open state and their relation to the domains that change conformation to form closed states are fundamental to the elucidation of the molecular mechanism of connexin voltage-gating at the atomic level.

A unique feature of connexin voltage-gating is that the voltage sensed by the charged amino acids forming a voltage sensor is that within the pore (11,12). Because both opening and closing are voltage-sensitive, the voltage-sensing residues must sense membrane voltage when the pore is closed as well as when it is open. This leads to the idea that the voltage sensors are also integrated into the permeability barriers, thereby stabilizing closed conformations and allowing voltage-driven opening.

Although the components of the loop-gate voltage sensor have not been identified, studies have shown that the loop-gate permeability barrier is formed by a segment (the parahelix) of the first extracellular loop at the border of the first transmembrane domain (TM1/E1) in both the chimeric Cx32*43E1 and Cx50 undocked hemichannels (13,14).

Submitted October 7, 2011, and accepted for publication February 7, 2012.

*Correspondence: ted.bargiello@einstein.yu.edu

Editor: Jose Faraldo-Gomez.

0006-3495/12/03/1341/11 $2.00

doi: 10.1016/j.bpj.2012.02.009

Channel closure is achieved by a conformational change that reduces pore diameter from ~20 Å to ≤4–5 Å in this region. Tang et al. (14) provide evidence that as the parahelix forms the loop-gate permeability barrier it undergoes a structural reorganization and/or an axial rotation from its open state conformation. Evidence was also presented that the TM1/E1 bend angle straightens with loop-gate closure, causing a change in TM1 tilt that would reduce the diameter of the intracellular entrance to the pore.

Remarkably, molecular dynamics (MD) simulations of the open Cx26 hemichannel have shown that the TM1/E1 segment that forms the permeability barrier is the most stable region of the open channel pore (15). This observation raises the question of how the large loop-gating conformational change is realized given the stability of the permeability barrier forming segments in the open state. Several hydrophobic and electrostatic interactions that potentially contribute to stability of the TM1/E1 pore region were identified by Maeda et al. (16), based on amino-acid proximities in the crystal structure of the Cx26 junctional channel. These included two hydrophobic cores formed by intrasubunit interactions and electrostatic interactions comprising both intra- and intersubunit interactions among groups of charged and polar residues in TM1/E1.

Although the Cx26 crystal structure was proposed to represent the structure of the open channel, calculations of ion flux with grand canonical Monte Carlo Brownian dynamics (17–20) strongly suggested that the pore diameter of the crystal structure, particularly in the region formed by the N-terminus, was too narrow to account for the experimentally observed ion flux (15). MD simulations relaxed the crystal structure by expanding the pore in the vicinity of the N-terminus and altering the tilt angles and packing of all four transmembrane helices, but notably the extracellular domains, which contact in the formation of the intercellular channel, did not change substantially. The I/V relations of the resulting average equilibrated structure calculated with grand canonical Monte Carlo Brownian Dynamics simulations closely matched experimentally observed I/V relations, when subsets of charge modifying co- and posttranslational modifications identified in Cx26 (22) were incorporated. Therefore, the average equilibrated structure more closely represents the open channel state than does the crystal structure.

Here, we reevaluate the crystal structure and determine the dynamic properties of the Cx26 hemichannel in the regions that form the loop-gate permeability barrier. The MD simulations identify extensive interconnected networks of van der Waals (vdW) and electrostatic interactions that stabilize the open state structure of the parahelix and the TM1/E1 bend angle. The analyses of MD trajectories show that thermal fluctuations within the electrostatic network lead to intra- and intersubunit structural fluctuations of the parahelix and hydrogen bonds that partially stabilize the TM1/E1 bend angle. Overall, the results suggest that transitions out of the open state are enabled by voltage-driven disruption of the electrostatic network and the resulting destabilization of the vdW networks. Furthermore, the presence of extensive intersubunit electrostatic connections that link all subunits together suggests that the loop-gate voltage sensor is effectively distributed over the six subunits in the parahelical region and that voltage-gating occurs by a concerted mechanism initiated by the structural reorganization of the stabilizing networks rather than by a simple, vectorial change in the position of a discrete voltage sensor in the electrical field.

MATERIALS AND METHODS

Molecular dynamics

The construction of the Cx26 system, based on PDB:2ZW3 of the Cx26 crystal structure, is described in Kwon et al. (15). Details are provided in the Supporting Material. Briefly, the Cx26 hemichannel was incorporated into an explicit, fully hydrated POPC membrane with 100 mM KCl and equilibrated by molecular dynamics (MD) simulation for 375 ps in CHARMM (23) followed by 140 ns in NAMD (24). After equilibration, four independent 20-ns production stage MD simulations were performed (initiated from different random seeds) to increase the probability that the system visited all possible conformational states. The double mutation, V43A+I74V, was produced by in silico mutagenesis of the equilibrated Cx26 hemichannel, followed by four independent 10-ns production stage MD simulations. Electrostatic and vdW energies were calculated in CHARMM (23,25).

Correlation analyses

Correlation analyses of wild-type and mutant channels were performed on 961 time series properties described in Results and Discussion. Pairwise correlations and cross correlations between time series properties were calculated using MATLAB (The MathWorks, Natick, MA).

RESULTS AND DISCUSSION

Structure and dynamic properties of the loop-gate permeability barrier (the parahelix) and the TM1/E1 bend angle

The segment of the channel pore formed by residues 42–51, located in E1 near the TM1 border, displays the smallest dynamic range in pore radius in MD simulations of the open state (Fig. 1, *A* and *B*) and lowest temperature factors (15) indicating that it is the most stable region of the open channel pore. However, this region undergoes a substantial conformational change when the channel is closed by voltage-dependent loop-gating (13,14).

The 42–51 segment contains a six-residue segment spanning V43–Q48, which was classified as a 3_{10} helix in the Cx26 crystal structure (16) (Fig. 1 *C*). This classification appears to be based on the pattern of backbone hydrogen bonding between residues 44 and 47 (44 ← 47), and between 48 and 51 (48 ← 51) in all six subunits of the crystal structure. However, the crystal structure shows no

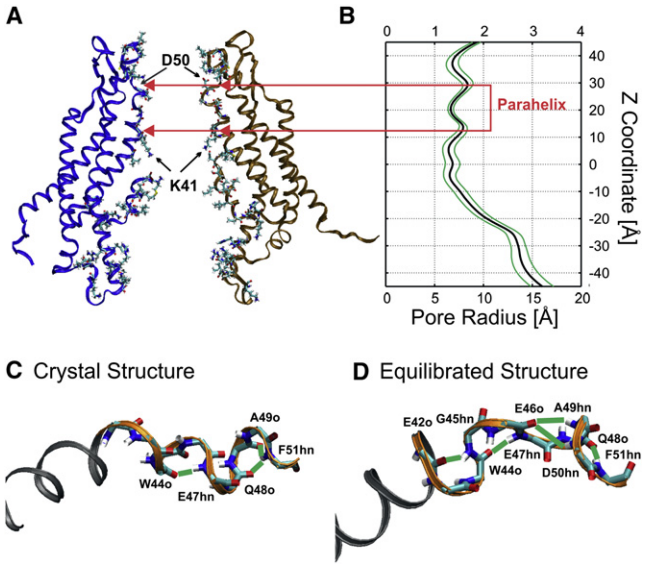

FIGURE 1 Structure of the parahelix formed by residues 42–51. (*A*) Side view of the "average equilibrated structure" showing the position of the parahelix. (*B*) The average pore radius calculated from the trajectories of the four production stage MD simulations. Standard deviation in pore radius determined with HOLE (31) (*green lines*). (*C*) Structure of the 42–51 segment in the Cx26 crystal. (*D*) The structure of the parahelix in the average equilibrated structure illustrating the formation of all observed hydrogen bonds (*green lines*).

hydrogen bonds between the backbone carbonyls and amide groups of residues 43 ← 46, 45 ← 48, 46 ← 49, or 47 ← 50, which are expected for a classical 3_{10} helix. After MD simulations, the pattern of backbone hydrogen bonding is expanded to include bonds between 42 ← 45, 44 ← 47, 46 ← 49, 46 ← 50, and 48 ← 51 (Fig. 1 *D*). The term "parahelix" has been proposed to describe an imperfect 3_{10} helix with characteristics similar to those evident in the equilibrated structures (26). Consequently, we refer to this domain as the 42–51 parahelix, noting that it includes the region described by Maeda et al. (16) as the 3_{10} helix. Although formation of these H-bonds fluctuates throughout the production-stage MD simulations (see Fig. S1 in the Supporting Material), these changes do not substantially change the pore diameter in this region (Fig. 1 *A*).

An extensive intrasubunit vdW network stabilizes the parahelix and TM1/E1 bend angle

Five nonpolar residues (V43, W44, G45, A49, and F51) are contained within the parahelix (Fig. 1 *D*). W44 and F51 and the nonpolar character of the 43rd residue are conserved among all members of the connexin family, whereas the 45th and 49th residues are often substituted with polar residues. G45 and A49 line the pore in both the crystal and MD equilibrated structures and have no interactions with other residues (15). V43 and W44 make intrasubunit contacts with other nonpolar residues within the interfaces of the four transmembrane helices.

We identified potential vdW interactions by first identifying amino-acid residues lying within 3 Å of residues V43, W44, and F51, as defined by an interaction list that is based on the position of all protein atoms throughout the four independent 20-ns production stage MD simulations (see the Supporting Material). An interaction list for the entire hemichannel is presented in Kwon et al. (15). In addition to V43 and W44, which fall within the 3 Å cutoff, these included five other residues: A39, F69, I74, M163, and F191. These primary interactions were extended to include secondary interactions with these five residues. This extended the network to include 12 additional residues, including I35, L36, V38, A40, Y65, Y68, I71, W77, L79, Y158, V182, and M195.

This interaction list includes the five residues, A39, A40, V43, W44, and I74 that were proposed from the crystal structure to form hydrophobic core 1 (16). Hydrophobic core 2 was proposed to be formed by interactions among residues W77, F154, and M195 (16). To facilitate comparisons of the crystal and equilibrated MD structures, these residues and their primary interactions involving residues I196 and L76 were included in the vdW interaction list. The third hydrophobic residue that is located in the parahelix, F51, is connected to the vdW network by a primary interaction with residue Y65. Primary interactions of Y65 with residues outside the network emanating from V43 and W44 were not considered.

The average vdW energies for pairs of residues were determined from the trajectories of the four replicate 20-ns production stage MD simulations. Because the calculation of these energies is computationally expensive, we limited our analyses to interactions among these 21 residues. A map of the identified vdW connections for the 21 residues is shown and compared to those in the crystal structure in Fig. 2. The time-averaged energy of individual interactions is shown in Fig. 2 *D* and Table S1 and Table S2 in the Supporting Material. A39 was removed from the interaction list as all its potential interactions (which include W44 and V43) had energies close to 0 kcal/mol, due to its distance from and few contact points with other nonpolar residues. Consequently, it was deemed not to contribute to the stability of the network.

The vdW network involves mostly intrasubunit interactions that primarily extend from the parahelix toward the intracellular end of the channel (Fig. 2). This network stabilizes the structure of the parahelix; primary interactions with parahelix residues V43, W44, and F51 contribute −7.46 kcal/mol/subunit. The network also links parahelix structure to the stability of the TM1/E1 bend angle via interactions with residues V38, L36, and I35 in TM1 across the TM1/E1 bend. These interactions contribute −3.77 kcal/mol/subunit.

The TM1/E1 bend angle is also stabilized by the formation of a backbone hydrogen bond between V43hn and A39o (see Fig. S2). In addition, salt bridges formed between

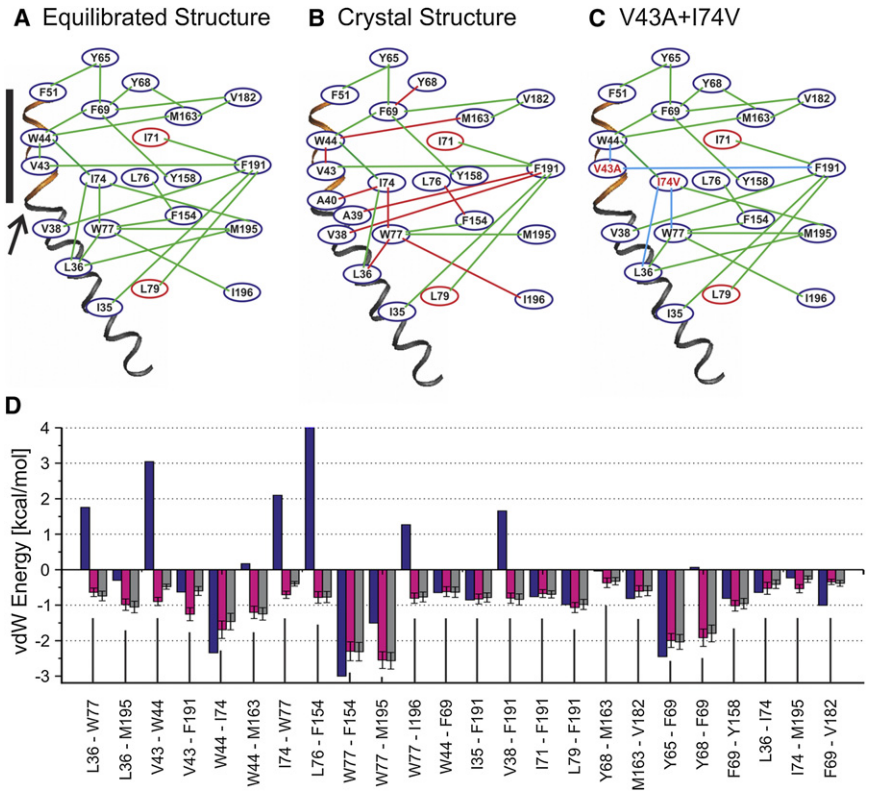

FIGURE 2 Map of the vdW networks extending from the parahelix through TM1. (*A*) Network determined from the trajectories of production stage MD simulations for the wild-type channel. Adjacent residues were included in the network if a portion of the time-averaged vdW energy was <-0.5 kcal/mol. (Connections of *blue ovals* by *green lines*) Intrasubunit interactions; (connections of *red ovals* to *blue ovals* by *green lines*) intersubunit interactions. (*B*) Network determined from the completed but unequilibrated Cx26 crystal structure. (*Red lines*) These connected residues in the vdW network depict residues that lie within 3.0 Å in the crystal structure but whose interactions have positive Lennard-Jones potentials. (*Green lines*) These connecting residues have vdW energies <-0.5 kcal/mol. (*C*) The network determined for the double mutation V43A+I74V from the trajectories of production stage MD simulations. (*Blue line*) Interactions that are substantially weakened from wild-type Cx26 (panel *A*). (*D*) vdW energies of specified interactions calculated in CHARMM from Lennard-Jones potentials: (*blue*) crystal structure; (*magenta*) equilibrated structures; (*gray*) double mutant. (*Solid bar*) Position of the parahelix; (*arrow*) TM1/E1 bend.

R32 (TM1) and E147 (TM3) as well as between K22 (TM1) and E209 (TM4) stabilize the position of N-terminal half of TM1 relative to the z axis of the channel pore and thereby would also stabilize the TM1/E1 bend angle. These stabilizing interactions display dynamic fluctuations during the course of the MD simulations (see Fig. S2), although there is little variability in the TM1/E1 bend angle around its mean value of 34.4° ± 4.2 over the course of production stage MD simulations (not shown).

The total energy of the vdW network of the dynamic structures shown in Fig. 2 *A* is −26.9 kcal/mol/subunit. In contrast, the energy of the network calculated for the Cx26 crystal structure (Fig. 2, *B* and *D*) is much higher, 1.6 kcal/mol/subunit (see the Supporting Material). The high energy value of the crystal structure is a consequence of the energetically unfavorable contacts depicted by the red lines in Fig. 2 *B*, which become favorable in the equilibrated structure. Overall, the crystal structure fails to identify many of the vdW interactions that form during MD equilibration because the Cx26 crystal structure positions some residues too close together, which not only result in positive energies, but also positions other residues too far apart, thus reducing their contribution to the total vdW energy.

Conservative amino-acid substitutions in the vdW network alter structure

Although most of the residues that form the vdW network are highly conserved among connexins, two residues, V43 and I74, are substituted with smaller nonpolar residues: A43 for V43 in Cx43 and Cx32*43E1, and V74 for I74 in Cx32, 30.3, 31.1, 25, 43, 32*43E1, and Cx47. The dynamics and role of the 43rd residue in loop gating is of particular interest. Tang et al. (14) reported that cysteine substitution of the 43rd residue (A43C) in the chimeric Cx32*43E1 hemichannel generated a high affinity Cd^{2+} binding site upon loop-gate closure, showing it moved into the channel pore, but was inaccessible to thiol modification with MTSEA-biotin-X when the channel was in the open state. This result was interpreted to indicate that the geometry of the parahelix changes with loop-gating by either axial rotation or disruption of its structure and suggests that interactions that stabilize the conformation of the parahelix are fundamental to understanding the molecular mechanism of loop-gating.

The map of the V43A+I74V vdW network after equilibration is presented in Fig. 2 *C*. Not surprisingly, the calculated interaction energy of the substituted residues, V43A and I74V, is increased (indicated by the *blue lines* in Fig. 2 *C* and Table S1 and Table S2). The increase is partly a consequence of the smaller side chains of the substituted residues, which decrease the number of contact points between interacting residues. The distance separating some of the interacting residues within the network decreases after equilibration, but in most cases the decrease in distance is insufficient to strengthen the vdW interactions to that of wild-type. The increase in this set of interactions

does not substantially change the strength of other interactions between other pairs of residues in the network (Fig. 2 *D*). However, the reduced vdW interaction between I74V and W77, which results from reduced numbers of contacts, is accompanied by slightly increased vdW interactions between W77 and L36, and W77 and M195.

The overall net effect of the V43A+I74V substitution is a small increase in the energy of the vdW network from -26.9 ± 0.16 kcal/mol/subunit in wild-type to -24.9 ± 0.15 kcal/mol/subunit. Although the overall energy of the network is changed only slightly, the repositioning of specific nonpolar residues caused by the double mutation have a substantial effect on the dynamics of some components of the electrostatic network, as described below in The Dynamic Properties of the Electrostatic Network are Changed by the V43A+I74V Mutation.

An extensive intra-/intersubunit electrostatic network stabilizes the parahelix and TM1/E1 bend angle

We utilized the same conceptual approach to define the electrostatic interactions emanating from the charged and polar residues in the parahelix. These include the highly conserved D46 and E47 residues and not conserved D50 and E42 residues.

Two separate electrostatic networks can be identified in the dynamic structures obtained with MD simulation. The first extends from D46 and E47 and includes salt-bridge and hydrogen-bond formation among subsets of residues in the group R75, R184, K188, E42, E187, and S72 (Fig. 3 *A*). The second, less extensive network involves only intersubunit hydrogen bonds formed between two residues contained in the parahelix, Q48 and D50 with N62 (Fig. 3 *B*).

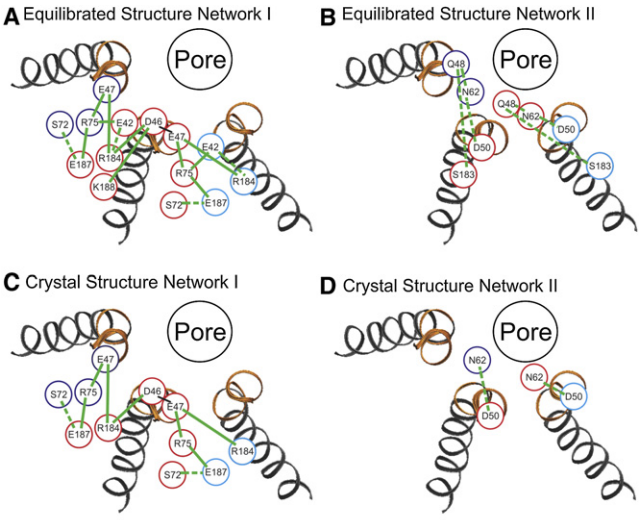

FIGURE 3 Map of two separate electrostatic networks traced from charged residues contained in the parahelix. (*A* and *B*) Electrostatic interactions in the MD equilibrated structures defined by the trajectories of production stage simulations. (*C* and *D*) Electrostatic interactions in the unequilibrated completed crystal structure. The positions of charged residues in three adjacent subunits are coded by differently color circles. (*Dotted green lines*) H-bonds; (*solid green lines*) salt bridges.

In contrast to the vdW network, which is formed primarily by intrasubunit interactions, the first electrostatic network involves both inter- and intrasubunit interactions (Fig. 3 *A*). A significant feature is the robust interconnection of intrasubunit interactions with intersubunit interactions that result in linkage among all six subunits. For example, the intrasubunit interaction of D46 with R184 is connected to both adjacent subunits by intersubunit interactions of R184 with E47. Similar interconnections of the intrasubunit interaction of E47 with R75 are mediated by intersubunit interactions of R75 with E42 and E187. Thus, the disruption of the electrostatic interactions within any subunit could disrupt the stabilizing electrostatic interactions of the network in all subunits. This suggests the possibility of a high degree of positive cooperativity such that changes in conformation in any given subunit will be transmitted to the two adjacent subunits. The second electrostatic network also has intersubunit interactions, but these are restricted to single adjacent subunits.

The electrostatic network of the crystal structure, based on our analysis of the PDB file, is shown in Fig. 3, *C* and *D*, and compared to the equilibrated structure in the Supporting Material.

Correlation analyses link the dynamics of the electrostatic network to that of the parahelix

A significant characteristic of the electrostatic network is that many of the electrostatic interactions represented in Fig. 3 *A* fluctuate between two or more conformations over time. This characteristic allowed us to ascertain whether these dynamic changes are linked to the structure and stability of the parahelix and TM1/E1 bend angle.

We performed a correlation analyses among 961 time series properties in each of the six channel subunits (5766 total) determined from their MD trajectories. These properties included: 1), All the electrostatic and vdW interactions described in the interaction lists provided in Kwon et al. (15) for the entire Cx26 hemichannel, which include those emanating from the parahelix. 2), The pitch, dihedral angles (Ψ/Φ), and side-chain bond torsion angles of the parahelix. 3), The solvent accessibility and pore-lining probability of all residues. 4), The TM1/E1 bend angle. 5), The tilt angle (with respect to the membrane-normal) of the four transmembrane helices. Fifty-five pairs of time series data had a correlation coefficient >0.70. These were assessed by cross-correlation analyses to identify correlated behaviors that were synchronized in time throughout the four replicate production stage simulations. (Details are described in the Supporting Material.)

Fig. 4 *A* shows the synchronized correlation map of electrostatic interactions in one of the six subunits emanating from E47, a residue located within the channel pore formed

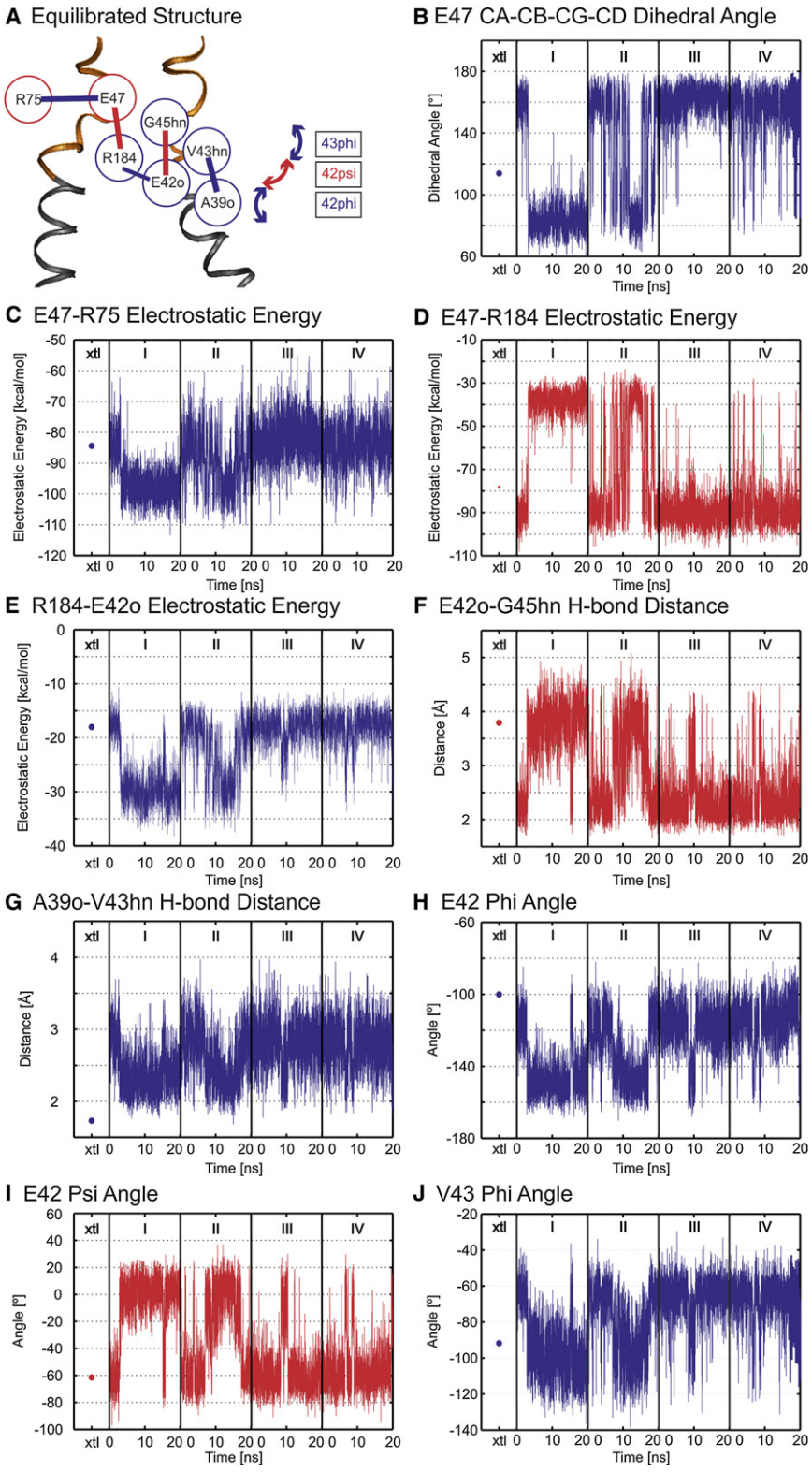

FIGURE 4 Correlation map of the electrostatic network derived from correlated time series of electrostatic interactions present between two adjacent subunits. (*A*) Correlation map of electrostatic interactions. (*Red* and *blue circles*) Residues located in adjacent subunits. (*B–J*) Time series properties of specified interactions. (*Blue*) All interactions positively correlated with that of E47-R75; (*red*) those that are negatively correlated (see text). (*Dots* in column *xtl*) Energies of the interactions determined for the unequilibrated crystal structure. Electrostatic energies were calculated from the Coulombic interactions between pairs of residues in vacuum ($\varepsilon = 1$).

by the parahelix. The time series of the properties shown in Fig. 4 *A*, which were identified by the cross-correlation analysis performed on 4–20-ns production stage simulations, are shown for the entire 140-ns equilibration stage simulation and production stage simulations in Fig. S3. This figure shows that the time series of properties were largely

asynchronous during the first 100 ns of the equilibration stage MD, but that fluctuations became synchronous in the 100–140-ns time interval and continued throughout the production stage simulations. The cross-correlation analysis of these time series properties of the four replicated 20-ns production stage MD simulations are shown in Fig. S4. Essentially, the same behavior was observed in the remaining five subunits, but in these, the fluctuations between conformational states were less frequent during the course of the four 20-ns production stage simulations and some time series properties were less perfectly synchronized (not shown).

The time series of components of the network shown in Fig. 4 *A* are highly synchronized (Fig. 4, *B–J*, and see Fig. S4). The correlations are color coded as follows: Time series properties positively correlated with the E47-R75 interaction are connected by a blue line and the corresponding time series properties are depicted in blue in Fig. 4. Time series properties negatively correlated with the E47-R75 time series are connected by a red line and depicted in red in Fig. 4. Thus, for example, an increase in the strength of the intrasubunit electrostatic interaction between E47 and R75 (*blue line*) results in a decrease in the intersubunit electrostatic interaction between E47 and R184 (*red line*), whereas the decrease in strength of the E47-R184 electrostatic interaction increases the probability of hydrogen-bond formation between the side chain of R184 and the backbone carbonyl of E42 (*blue line*). The second electrostatic network did not participate in any correlated behaviors, nor did any other pairs of the 961 time series properties analyzed display synchrony with the correlated network shown in Fig. 4.

The significant feature revealed by the correlation analysis is that changes of the strength of electrostatic interactions in one subunit causes changes in the stabilizing interactions and structure of the loop-gating elements in the adjacent subunit. These include changes in the pattern of backbone hydrogen bonds and Ψ- and Φ-angles that define the structure of the parahelix, as well as in the dynamics of the backbone hydrogen bond (A39o ← V43hn) that stabilizes the TM1/E1 bend angle. Thus, changes in electrostatic interactions can be directly related to the structure of the parahelix, and due to intersubunit contacts, could propagate throughout the hexameric channel. We do not assert that the correlation network defines the molecular path linking open and loop-closed state structures; however, it is likely to play a significant role in the initiation of voltage-dependent loop-gating, as discussed below.

The dynamic properties of the electrostatic network are changed by the V43A+I74V mutation

Because the time series of vdW interactions did not display distinct steps between conformations, potential relations between the vdW network and other elements could not be established with a correlation analysis. We explored possible interactions of the vdW and electrostatic networks by examining the dynamics of the electrostatic network in the V43A+I74V channel. As described above, these mutations map to key residues within the vdW network and produce changes in vdW interactions, decreasing the interaction of specific pairs and slightly increasing the interaction other pairs (Fig. 2).

The electrostatic interactions involving E42, E47, R75, and R184 are shown in Fig. 5, *A* and *B*, for wild-type and the double mutant, respectively. Although the double mutation does not cause new interactions to form or delete existing ones, it changes the dynamics of the interactions between E47-R75 and R184-E42o by reducing the flexibility of side chain of R75 (Fig. 5, *C* and *D*). The reduced flexibility is a consequence of the reduced volume of the space enclosing the side chains of E42, E47, R75, and R184 (Fig. 5, *E* and *F*), which results from the decreased distance between A43 and F191 (Fig. 5, *G* and *H*). Remarkably, the decreased distance is insufficient to compensate for the large increase in the energy of this vdW interaction (Fig. 2 *D*). Notably, the distance between W44 and mutant V74 does not change although the interaction is characterized by reduced numbers of contacts.

The consequence of these changes is that rather than transiting between only two conformational states, evident in the time series of E47-R75 and R184-E42o for wild-type Cx26 (Fig. 4, *C* and *E*), the mutant channel also adopts a novel metastable conformation (state 2 in Fig. 6). In this conformation, a single hydrogen bond forms between E47 and R75 (E47 OE1 and either R75 HH11 or R75 HH21: or E47 OE2 and either R75 HH11 or R75 HH21). This contrasts with the structure of the more stable state, in which two hydrogen bonds are simultaneously formed between E47 OE1 and E47 OE2 with R75 HH11 and R75 HH21 (Fig. 6 *E*).

Thus, the double mutation not only reduces the strength of vdW interactions arising from V43A, but also changes the dynamic behavior of a specific set of electrostatic interactions that are linked to the stability of structure of the parahelix and TM1/E1 bend angle. Such a change, due entirely to conservative, hydrophobic substitutions, could alter the sensitivity of the electrostatic network to voltage.

Implications for voltage dependent loop-gating

The loop-gate voltage sensor

The correlation analysis demonstrates that, even within the open state, dynamic changes in interactions within the electrostatic network affect the parameters that define the structure of the parahelix. Thus, disruption of the open state electrostatic network in response to voltage should greatly affect the structure and stability of the parahelix.

All available data indicate that the voltage sensors of connexin channels are located within the aqueous pore, in both

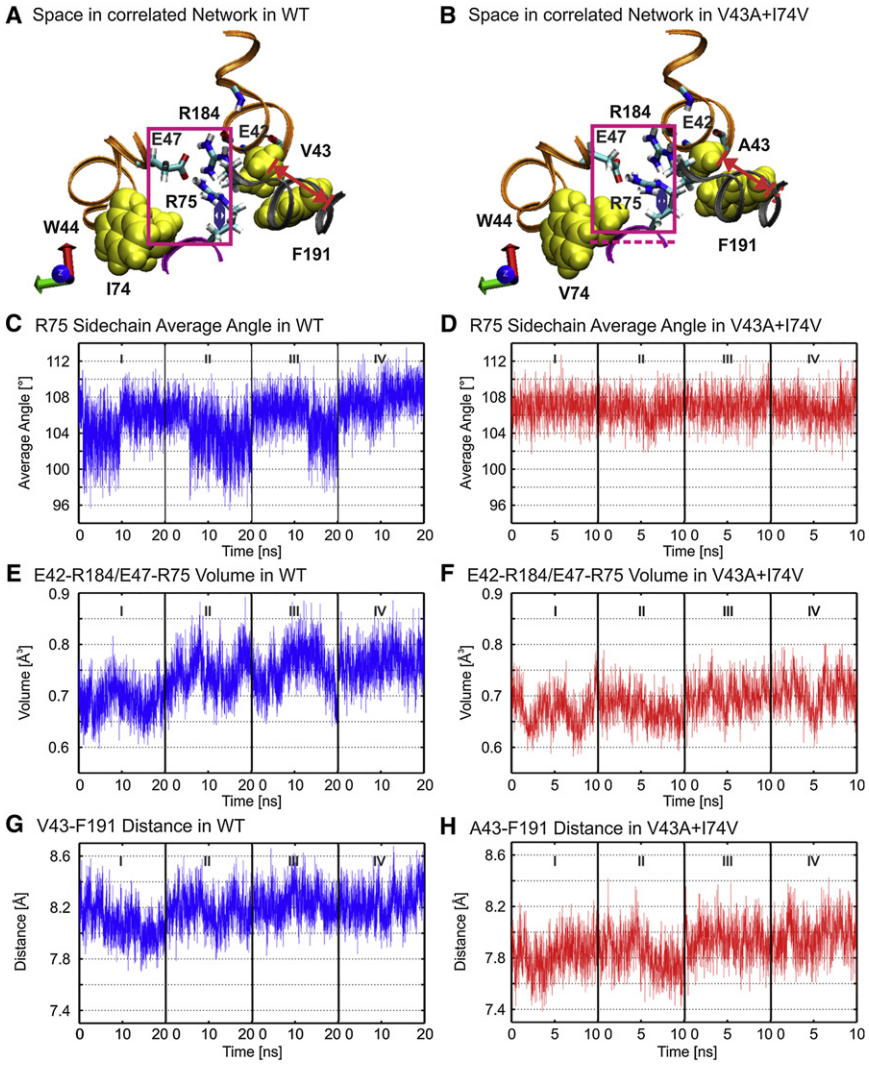

FIGURE 5 Double-mutation V43A+I74V changes electrostatic interactions by reducing the volume of empty space. (*A* and *B*) The position of interacting charged residues in wild-type and double mutant. (*Magenta box*) Face view of cube defined by Cα of E42, E47, R75, and R184. The dashed magenta line in *B* is the lower boundary of the box shown in *A*. (*Red dashed line*) Distance measured between the Cα carbons of A43 and F191. The red dashed line in *B* marks the position of the Cα of F191 in panel *A*. (*C* and *D*) Averaged time series of the angles and dihedral angles of the R75 side chain of wild-type and double mutant. (*E* and *F*) Time series of the volume of the cubes depicted by the magenta boxes in *A* and *B*. (*G* and *H*) Times series of the distance between Cα of V43 and F191 in wild-type and double mutant. The distance measured is shown by the red lines in *A* and *B*.

open and closed states (12). Of the charged residues that comprise the electrostatic network, E42, D46, E47, D50, R184, and K188 lie within or immediately adjacent to the pore. Because D46 and E47 are in the parahelix, they will be in the pore when the loop gate is closed, providing a means by which voltage and divalent cations can stabilize the closed state.

Because the electrostatic network contains charges positioned to sense voltage in open and closed states, and it stabilizes the open conformation of the parahelix, we propose that the network, which is formed by both inter- and intrasubunit interactions, comprises the voltage-sensor for loop-gating. In the simplest case, inside negative voltage would initiate loop-gating by destabilizing the network by inward movement of positive charges and outward movement of negative charges.

With the exception of E42 and D50, the charged residues contained within the electrostatic network of the Cx26 hemichannel are highly conserved. Conservation of these charged residues is congruent with the conserved polarity of loop-gating among all connexins.

Formation of the gate

The correlation analysis demonstrates that dynamic changes in interactions of several components of the electrostatic network are directly related to parameters that define the structure of the parahelix and to the stability of the TM1/E1 bend angle, both of which have been shown to change conformation with loop-gate closure (14). We propose that the loop-gate permeability barrier results from disruption of the structure of the parahelices, allowing them to adopt a geometry that protrudes into the channel pore (see Fig. S5). This mechanism allows the conformational changes to be local to the TM1/E1 region and not to require large-scale reorganization of interactions among transmembrane helices. Straightening of the TM1/E1 bend angle with loop-gate closure is likely a consequence of the reorganization of the vdW and

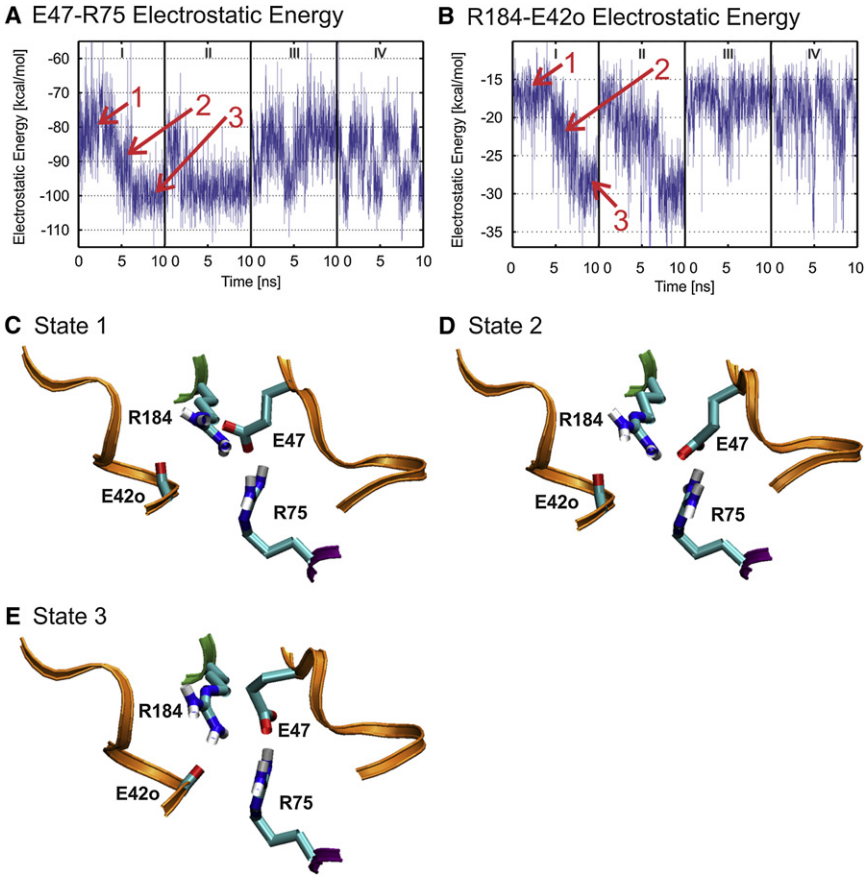

FIGURE 6 V43A + I74V alter the dynamics of electrostatic interactions. (*A* and *B*) Time series of E47-R75 and R184-E42o electrostatic energies, respectively, demonstrate the presence of three distinct conformational states in the double mutant. The intermediate conformation, 2, is never observed in the time series of wild-type (see Fig. 4, C and *E*). (*C*) The conformation of the channel when it resides in high energy state 1. (*D*) The conformation of the channel when it resides in the lower intermediate energy state 2. (*E*) The conformation of the channel when it resides in the low energy state 3. The conformations of states 1 and 3 are essentially identical to the conformations adopted by the wild channel (not shown).

electrostatic interactions that accompany the conformational change in the parahelix.

Concerted gating

The remarkable feature of the first electrostatic network (Fig. 3 *A*) is that it extends across subunit boundaries in both directions and links all subunits, providing a thermodynamic basis for highly cooperative interactions in the destabilization (and stabilization) of the open loop-gate conformation. The positive cooperativity could operate in two ways: positive cooperativity among the subunits (e.g., destabilization in one subunit lowers the transition energy for destabilization in other subunits), and/or positive cooperativity of disruption of the electrostatic networks, effectively making a single loop-gate voltage sensor for the whole hexameric channel. In the former case, the intermediate states seen in single-channel transitions would correspond to participation of increasing numbers of parahelices in occluding the pore. In the latter case, they would correspond to the linked electrostatic networks stepping together through a series of intermediate structures, each of which increases pore occlusion. Though data do not allow these mechanisms to be distinguished, we favor the latter, because the intrasubunit and intersubunit character of the electrostatic network suggests coordinated reconfiguration of the whole system.

Voltage-dependent stabilization-destabilization of the open state

The slow time constant of Cx26 loop-gating (in the range of seconds at −90 mV (9,10) suggests that the open and loop-gate closed states are separated by a substantial energy barrier, when interpreted in terms of transition state theory. Although any given vdW interaction is small, in the range of −0.5 to −3 kcal/mol (Fig. 2 *D*), the contribution of the network is substantial, −26.9 kcal/mol/subunit. If one considers only the primary vdW interactions extending from V43 and W44 and F51, the calculated average vdW energy is −7.46 kcal/mol/subunit. The vdW energy of primary interactions that stabilize the TM1/E1 bend is −3.77 kcal/mol/subunit.

It is difficult to assess the contributions of individual electrostatic interactions to the energy of the open state, because the calculation depends on the dielectric value of the medium between the interacting residues. However, we note that several interactions, including E47 with R184, E47 with R75, and D46 with R184 and K188, are broken and reformed with only the thermal energy provided by

the simulation (0.62 kcal/mol at 310 K). This suggests that the open state is stabilized by the additive effect of multiple weak electrostatic interactions. Only the R75-E187 and R75-E42 interactions are stable throughout the MD simulations.

Because the open state is stabilized by many relatively weak interactions, we propose that the transition to the loop-gate closed state most likely proceeds by the sequential destabilization of open-state interactions and formation of new interactions that stabilize the transition and closed states. This view is analogous to the concept of a conformational wave that has been proposed to underlie activation of ligand-gated channels (27–30). In the case of connexin channels, the conformational wave would be initiated by the movement of some of the residues that comprise the loop-gate voltage sensor, many of which are stabilized by energies <2.3 kcal/mol that would be provided to each charged residue by a 100-mV polarization. It is likely that the first interactions to be disrupted would be weakest, such as those mentioned above.

CONCLUSIONS

Equilibration of the Cx26 hemichannel crystal structure by all-atom MD simulations results in the reorganization of amino-acid interactions in a region of the first extracellular loop, here termed the "parahelix". This domain undergoes large conformational changes when the connexin hemichannels transit from the open to the loop-gate closed conformation, yet it is the most stable region of the channel pore. The open channel structure of the parahelix is stabilized by two large interconnected networks—a vdW network and an electrostatic network. Both networks are much larger than was inferred from the distance measurements in the crystal structure (16), reflecting the repositioning of interacting residues to optimize their interactions in MD simulations. Importantly, the stabilizing electrostatic network spans adjacent connexin subunits, suggesting highly cooperative (concerted) loop-gating transitions.

Several of the charged residues contained within the network are located in the open channel pore as required for a connexin voltage sensor, and two are positioned within the parahelix, where they would continue to sense voltage when the channel is closed. We conclude that the electrostatic network forms a portion of (if not all) the loop-gate voltage sensor. The positions and interactions among these charged residues are consistent with the expectation that voltage acts to destabilize the open state and to stabilize the closed state of the channel.

Although the MD simulations do not describe the sequence of gating transitions linking the open and closed states, they demonstrate several features that are likely to be relevant to the conformational changes underlying voltage-dependent loop-gating:

1. Dynamic changes in interactions within the electrostatic network correlate with dynamic changes in the structure of the parahelix, suggesting that the structure of the loop-gate permeability barrier is a function of the structural organization of the voltage sensor.
2. The electrostatic interactions linked to the parahelix involve both inter- and intrasubunit interactions that interconnect the six subunits. Thus, changes in the conformation of parahelix in one subunit will determine the stability of the parahelices in neighboring subunits. This strongly suggests that the loop-gate voltage sensor is not contained within an individual subunit, or at the interface of adjacent subunits, but rather, is a property of the entire hemichannel. This organization favors a concerted gating mechanism involving simultaneous conformational changes in all six subunits, as a consequence of positive cooperativity.
3. Dynamic fluctuations in the pattern of backbone hydrogen bonding and Ψ/Φ angles of the parahelix provide a measure of helical distortions that are related to the formation of bends and changes in pitch. Distortions of parahelical geometry suggest a mechanism for pore diameter reduction by allowing the parahelix to adopt a conformation that would cause it to protrude into the channel pore, thus forming the permeability barrier with minimal energy cost.
4. The vdW network and electrostatic networks also contribute to the stability of the TM1/E1 bend angle. Thus, the reorganization of these networks when the channel adopts the closed conformation could change the TM1/E1 bend angle, narrowing the cytoplasmic entrance of the channel pore.
5. Mutations that decrease the stability of the vdW network can change the dynamics of specific sets of interactions in the electrostatic network, thus potentially changing the network's sensitivity to voltage. The two networks are interconnected: changes in the conformation of the voltage sensor could result in the reorganization of the vdW network, and, conversely, changes in the vdW network resulting from mutations of nonpolar residues could change the dynamics of the electrostatic network.
6. We propose that loop-gating is initiated by movement of charged residues contained within the electrostatic network. The action of voltage on the loop-gate voltage sensor is to disrupt the thermodynamically linked networks that stabilize the open channel structure of the parahelix and the TM1/E1 bend angle. We suggest that the large energy barrier separating the open and closed states is crossed by passage through a series of concerted small voltage-dependent intermediate steps analogous to a conformational wave proposed to operate in opening and closing of ligand-gated channels (27).

SUPPORTING MATERIAL

Completion of crystal structure and construction of the simulation system, molecular dynamics simulations, construction of interaction lists, calculation of van der Waals and electrostatic interactions, and five figures, d two tables, and references are available at http://www.biophysj.org/biophysj/supplemental/S0006-3495(12)00209-3.

We thank Dr. Wonpil Im, University of Kansas, for assistance and advice in constructing the computational systems used in this study. The computational aspects of this work were performed on the IBM iDataPlex Cluster managed by the Division of High Performance and Research Computing at the University of Medicine and Dentistry of New Jersey and is gratefully acknowledged.

Additional computational resources were provided by the National Science Foundation through TeraGrid resources provided by the National Center for Supercomputing Applications under grant TG-IBN090012 and by the High Performance Computing Core Service at the Albert Einstein College of Medicine. This work was supported in part by the National Institutes of Health under grants RO1 NS056509 to A.L.H., RO1 GM064889 to T.A.B., and RO1 GM062342 to B.R. Additional financial support from the Albert Einstein College of Medicine to T.A.B. is gratefully acknowledged.

REFERENCES

1. Trexler, E. B., M. V. Bennett, …, V. K. Verselis. 1996. Voltage gating and permeation in a gap junction hemichannel. *Proc. Natl. Acad. Sci. USA.* 93:5836–5841.
2. Oh, S., C. K. Abrams, …, T. A. Bargiello. 2000. Stoichiometry of transjunctional voltage-gating polarity reversal by a negative charge substitution in the amino terminus of a connexin32 chimera. *J. Gen. Physiol.* 116:13–31.
3. Bukauskas, F. F., and V. K. Verselis. 2004. Gap junction channel gating. *Biochim. Biophys. Acta. Biomembranes.* 1662:42–60.
4. Verselis, V. K., and M. Srinivas. 2008. Divalent cations regulate connexin hemichannels by modulating intrinsic voltage-dependent gating. *J. Gen. Physiol.* 132:315–327.
5. Gómez-Hernández, J. M., M. de Miguel, …, L. C. Barrio. 2003. Molecular basis of calcium regulation in connexin-32 hemichannels. *Proc. Natl. Acad. Sci. USA.* 100:16030–16035.
6. Oh, S., Y. Ri, …, T. A. Bargiello. 1997. Changes in permeability caused by connexin 32 mutations underlie X-linked Charcot-Marie-Tooth disease. *Neuron.* 19:927–938.
7. Bukauskas, F. F., A. B. Angele, …, M. V. Bennett. 2002. Coupling asymmetry of heterotypic connexin 45/connexin 43-EGFP gap junctions: properties of fast and slow gating mechanisms. *Proc. Natl. Acad. Sci. USA.* 99:7113–7118.
8. Rackauskas, M., M. M. Kreuzberg, …, F. F. Bukauskas. 2007. Gating properties of heterotypic gap junction channels formed of connexins 40, 43, and 45. *Biophys. J.* 92:1952–1965.
9. Gonzalez, D., J. M. Gomez-Hernandez, and L. C. Barrio. 2006. Species specificity of mammalian connexin-26 to form open voltage-gated hemichannels. *FASEB J.* 20:2329–2338.
10. Sánchez, H. A., G. Mese, …, V. K. Verselis. 2010. Differentially altered Ca^{2+} regulation and Ca^{2+} permeability in Cx26 hemichannels formed by the A40V and G45E mutations that cause keratitis ichthyosis deafness syndrome. *J. Gen. Physiol.* 136:47–62.
11. Harris, A. L., D. C. Spray, and M. V. Bennett. 1981. Kinetic properties of a voltage-dependent junctional conductance. *J. Gen. Physiol.* 77:95–117.
12. Bargiello, T., and P. Brink. 2009. Voltage-gating mechanisms of connexin channels. *In* Connexins. A. L. Harris and D. Locke, editors. Humana Press, Totowa, NJ. 103–128.
13. Verselis, V. K., M. P. Trelles, …, M. Srinivas. 2009. Loop gating of connexin hemichannels involves movement of pore-lining residues in the first extracellular loop domain. *J. Biol. Chem.* 284:4484–4493.
14. Tang, Q., T. L. Dowd, …, T. A. Bargiello. 2009. Conformational changes in a pore-forming region underlie voltage-dependent "loop gating" of an unapposed connexin hemichannel. *J. Gen. Physiol.* 133:555–570.
15. Kwon, T., A. L. Harris, …, T. A. Bargiello. 2011. Molecular dynamics simulations of the Cx26 hemichannel: evaluation of structural models with Brownian dynamics. *J. Gen. Physiol.* 138:475–493.
16. Maeda, S., S. Nakagawa, …, T. Tsukihara. 2009. Structure of the connexin 26 gap junction channel at 3.5 Å resolution. *Nature.* 458:597–602.
17. Egwolf, B., Y. Luo, …, B. Roux. 2010. Ion selectivity of α-hemolysin with β-cyclodextrin adapter. II. Multi-ion effects studied with grand canonical Monte Carlo/Brownian dynamics simulations. *J. Phys. Chem. B.* 114:2901–2909.
18. Lee, K. I., H. Rui, …, W. Im. 2011. Brownian dynamics simulations of ion transport through the VDAC. *Biophys. J.* 100:611–619.
19. Im, W., S. Seefeld, and B. Roux. 2000. A grand canonical Monte Carlo-Brownian dynamics algorithm for simulating ion channels. *Biophys. J.* 79:788–801.
20. Noskov, S. Y., W. Im, and B. Roux. 2004. Ion permeation through the alpha-hemolysin channel: theoretical studies based on Brownian dynamics and Poisson-Nernst-Plank electrodiffusion theory. *Biophys. J.* 87:2299–2309.
21. Reference deleted in proof.
22. Locke, D., S. Bian, …, A. L. Harris. 2009. Post-translational modifications of connexin26 revealed by mass spectrometry. *Biochem. J.* 424:385–398.
23. Brooks, B. R., C. L. Brooks, 3rd, …, M. Karplus. 2009. CHARMM: the biomolecular simulation program. *J. Comput. Chem.* 30:1545–1614.
24. Phillips, J. C., R. Braun, …, K. Schulten. 2005. Scalable molecular dynamics with NAMD. *J. Comput. Chem.* 26:1781–1802.
25. Brooks, B. R., R. E. Bruccoleri, …, M. Karplus. 1983. CHARMM: a program for macromolecular energy, minimization, and dynamics calculations. *J. Comput. Chem.* 4:187–217.
26. Enkhbayar, P., K. Hikichi, …, N. Matsushima. 2006. 310-Helices in proteins are parahelices. *Proteins: Struct., Funct., Bioinform.* 64:691–699.
27. Grosman, C., M. Zhou, and A. Auerbach. 2000. Mapping the conformational wave of acetylcholine receptor channel gating. *Nature.* 403:773–776.
28. Auerbach, A. 2003. Life at the top: the transition state of AChR gating. *Sci. STKE.* 2003:re11.
29. Purohit, P., and A. Auerbach. 2007. Acetylcholine receptor gating: movement in the α-subunit extracellular domain. *J. Gen. Physiol.* 130:569–579.
30. Purohit, P., and A. Auerbach. 2007. Acetylcholine receptor gating at extracellular transmembrane domain interface: the "pre-M1" linker. *J. Gen. Physiol.* 130:559–568.
31. Smart, O. S., J. G. Neduvelil, …, M. S. Sansom. 1996. HOLE: a program for the analysis of the pore dimensions of ion channel structural models. *J. Mol. Graph.* 14:354–360, 376.